Simulation Analysis of Optimal Camera Viewpoints for Glossy-Surface Inspection

K. Tanaka, *Member, IAENG*

***Abstract*—One of the primary applications of machine vision is automating the visual inspection of industrial products. Significant advancements have been made in the development of the technology. However, the inspection for certain difficult-to-detect defects (such as shallow concave defects on glossy surfaces) has not yet been automated. However, visual inspectors know from experience that slight irregularities are easier to perceive when the viewpoint is held just above the surface. This study analyzes the effect of this "just above the surface view" on the visualization of defects through optical simulation analysis. Additionally, it clarifies that a lower viewpoint is not always optimal, depending on the degree of inclination of the defect surface. The new findings presented in this paper can contribute to the optimal design of the optical system of a visual inspection system.**

***Index Terms*—automated surface inspection, image detection, optical simulation, visibility**

I. Introduction

AUTOMATED surface inspection using machine vision is an important task in the manufacturing industry. Surface inspection covers the surfaces of various materials such as metals, plastics, and ceramics. The process entails the detection of several types of defects, such as irregularities (concave and convex), stains, and abrasions. Many studies have been conducted to optimize inspection methods for specific materials, surface shapes, and defect types [1]–[4]. This study focuses on the automatic inspection for uneven defects on glossy surfaces such as polished metals and painted surfaces.

The image detection method for irregular defects (concave and convex) is based on the fact that the normal direction of the surface of an irregular defect is significantly different from that of the surrounding normal surface. In this method, the manner in which the test surfaces are illuminated with light is important, and there are two main methods: dark-field illumination and bright-field illumination. Dark-field illumination is a method in which the camera and light source are arranged such that the specular reflection of the light source on the normal surface of the object falls outside the field of view of the camera (Fig. 1). In this case, defect detection constituted image detection using the light reflected by irregular defects. It is necessary to find a way to prevent the light reflected by normal surfaces from entering the field of view of the camera, and an optical system that masks the specular reflected light was proposed in [5].

Manuscript received March 28, 2024; revised September 27, 2024.

K. Tanaka is a professor of Kindai University, Hiroshima, 739-2116 Japan. (phone: +81-82-4347384; e-mail: kazumoto@hiro.kindai.ac.jp).

Bright-field illumination is the opposite of dark-field illumination, in which light reflected from a normal surface enters the field of view of the camera. Consequently, the light reflected from the defect was not captured by the camera because the normal direction of the defect area was different from that of the surrounding area, and the image of the defect was darker than that of the surrounding area, thus enabling defect detection (Fig. 2). Dark-field illumination allows the camera to capture the light reflected by part of the defect, whereas bright-field illumination has many applications because it is easier to obtain the overall shape of the defect. However, simply increasing the size of the light source to inspect a large area makes it difficult to detect defects (see the caption in Fig. 2). Therefore, systems have been developed to scan objects without increasing the size of the light source while moving the object [6] or moving the camera and light source set [7]. Alternatively, structured light, such as striped patterns, can be used instead of a uniform light source. The light source can be extended because the pattern distortion that occurs in the defect area can be detected. Many studies have been conducted on defect detection using this method, including those that employed wavelets [8]–[10], structured functions [11], and feature extraction using deep neural networks (DNN) [12]. In addition, phase-measuring deflectometry (PMD), a technique that uses structured light to measure the surface topography in three dimensions (3D), has been investigated for defect detection [13],[14].

However, the automatic detection of very shallow concavities remains challenging. However, visual inspectors know from experience that slight irregularities are easier to observe when the viewpoint is held just above the surface, as shown in Fig. 4. Equation (1) is the Beckmann–Spizzichino roughness parameter g [15], which expresses the roughness of an object surface; the smaller the value, the more specular the surface.

$$g = \left(4\pi\sigma\frac{(\cos\theta_i+\cos\theta_r)}{\lambda}\right)^2 \quad (1)$$

where σ, λ, θ_i, and θ_r are the standard deviation of the amount of irregularity (μm), the wavelength of the incident light (μm), the angle between the incident ray and the normal, and the angle between the reflected ray and the normal, respectively. From (1), assuming that σ and λ are constant, the closer θ_i and θ_r are to $\pi/2$, the higher the specular reflectance. The effect of the "looking from just above the surface" is thought to be because of the increased reflectivity of surfaces, which makes it easier to detect slight irregularities in reflectance [16]. Images of a specular surface with a slight concave defect captured from two different viewpoints under bright-field illumination using a stripe-pattern light source are shown in Fig. 5. As mentioned above, the figure shows that the stripe pattern is more visible in the

"looking from just above the surface" case than in the other case. Not only that, but in the "looking just above the surface" case, the pattern distortion caused by the concavity appears to be greater in the image. This phenomenon is expected to be useful in the design of optical systems for automatic inspection equipment.

This study addresses the following research questions that arose while automating the visual inspection of slight concaves that occur during the press forming of mirror-finished press-formed products.

- Is defect visualization by "looking from just above the surface" always effective regardless of surface curvature or defect size?
- Is a lower viewpoint height from the surface more effective for visualizing defects?

This study provides answers to these questions using an optical simulation method for bright-field illumination with a stripe-pattern light source.

Several optical simulations for the optimal design of stripe-pattern light-surface measurement systems have been reported in previous studies. In [17], the optimal width of the stripe for visualizing unevenness was analyzed using an optical simulation. A simulation analysis of the optimal design of the optics in a PMD was conducted [18]. In [19], curved stripe patterns were analyzed via simulation to extend the inspection range of the PMD. The distinctive feature of this study is that it does not analyze stripe patterns but clarifies the relationship between the height of the camera from the surface and the visibility of defects.

The main contributions of the study are as follows:

- We reveal that the optimal viewpoint height for visualizing defects caused by stripe-pattern distortion depends on the degree of defect inclination.
- It has been found that the height of the viewpoint that is suitable for visualization tends to be the same regardless of whether the object is flat or curved.
- Shallow defects are difficult to visualize, but "looking from just above the surface" was found to be the most effective visualization method for shallow defects.

The remainder of this paper is organized as follows. Section II describes the ray-tracing method for bright-field illumination using a stripe-pattern light source. The results of the simulation are presented in Section III. In Section IV, the effects of viewpoint height are discussed. Section V concludes the paper and provides directions for future research.

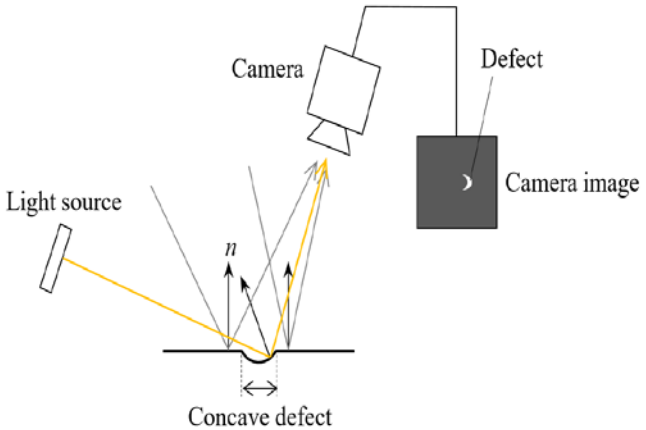

Fig. 1 Dark-field illumination.

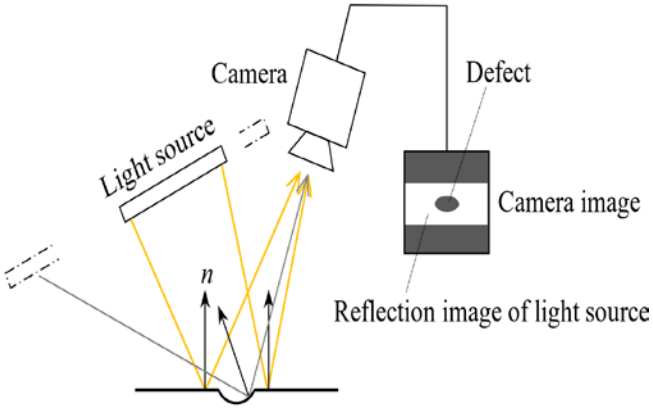

Fig. 2 Bright-field illumination. The single dotted line represents part of the light source when extended; when extended in this way, the defect is not visible because the defect also reflects light from the light source towards the camera.

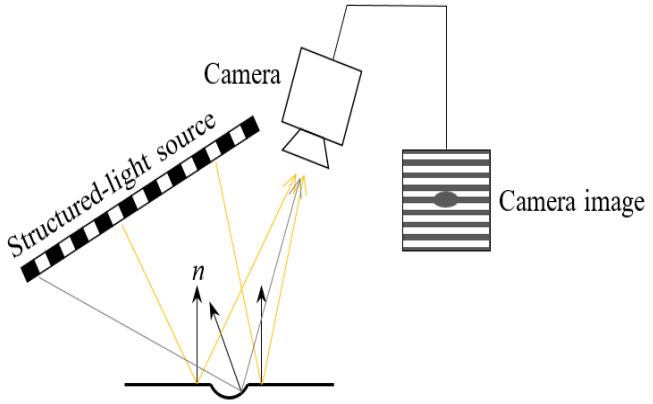

Fig. 3 Bright-field illumination using structured-light source.

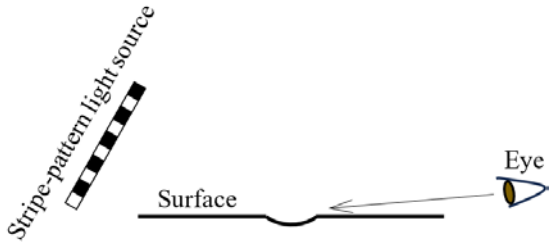

Fig. 4 Visual inspection by "looking from just above the surface."

Fig. 5 (Left) Image taken with the camera's viewpoint set to "just above the surface." At the back is a stripe-pattern light source. (Right) Image of the same object when the angle between the camera's line of sight and the normal is set to almost zero.

II. Method

This section describes the optical simulation and defect visibility evaluation methods used to address the research questions.

A. *Optical simulation*

The striped-pattern light source, test surface, and camera were arranged to enable bright-field illumination, as shown in Fig. 6. To simulate a situation in which defects are detected by an experienced inspector through an examination of the surface from a specific gazing point, the center point of one concave defect was placed at a designated gazing point on the optical axis of the camera.

The shape of the defect was represented by a two-dimensional Gaussian function in accordance with a previous study on the simulation of concave defect visualization [17]. Introducing a coordinate system with this center point as the origin and the plane containing the optical axis and the normal of the light source as the yz plane (Fig. 6), the defect is represented by (2).

$$y = -d_{max} e^{-\frac{1}{2}(x,\ z)\begin{pmatrix}{\sigma_x}^2 & \sigma_{xz} \\ \sigma_{zx} & {\sigma_z}^2\end{pmatrix}^{-1}(x,\ z)^{\mathrm{T}}}, \quad (2)$$

where ${\sigma_x}^2$ and ${\sigma_z}^2$ are the variances, σ_{xz} and σ_{zx} are the covariances, and d_{max} is the maximum defect depth. In the experiment, however, equal variances (${\sigma_x}^2 = {\sigma_z}^2 = \sigma^2$, $\sigma_{xz} = \sigma_{zx} = 0$) were assumed.

The shape of the test surface is expressed in the form of (3) such that flat and free-form surfaces can be represented.

$$y = f(x, z) \quad (3)$$

Thus, the sum of equations (2) and (3) represents the test surface containing the defect.

Camera images were simulated using backward ray tracing [20]. Specifically, the camera was a pinhole model, and when a ray connecting a pixel of the image sensor and the principal point reached the light source by specular reflection on the test surface, the brightness at the point of arrival was used as the pixel density. The brightness distribution of the striped pattern of the light source was approximated using a Gaussian distribution. The Blinn–Phong reflection model [21] was used to model the specular reflections on the surface. It was assumed that there was a blackout curtain in the background of the light source and that the rays that strayed from the light source reached the curtain. An example of the simulation results when the test surface was flat is shown in Fig. 7.

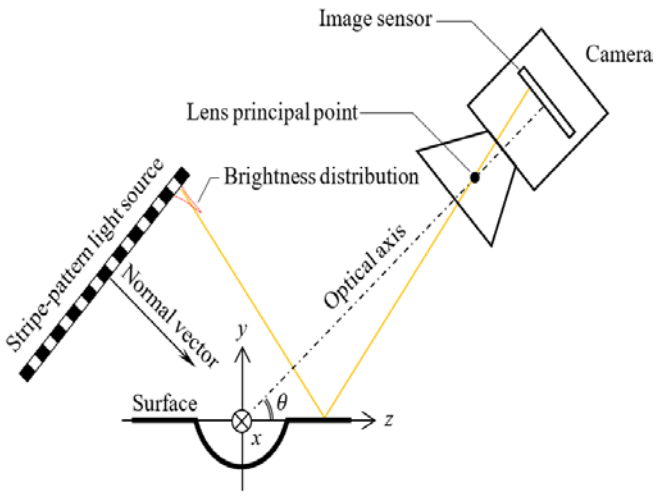

Fig. 6 Overview of the simulation model.

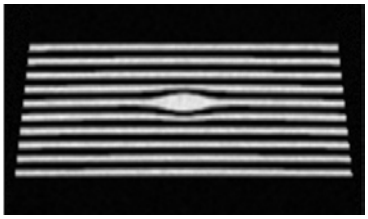

Fig. 7 Example of simulated camera image. Deformation of the striped pattern indicates a defect.

B. *Defect visibility evaluation method*

This subsection describes the method for evaluating the visibility of defects in defect images obtained via optical simulation. Because defects are visualized by the distortion of the stripe pattern image, the difference between the stripe pattern images of a defect-free surface (i.e., $d_{max} = 0$) and a surface with a concave defect was used to evaluate defect visibility. The evaluation procedure was as follows:

Step 1) Set $visibility$ to 0.
Step 2) The simulator generates images with and without a defect.
Step 3) Binarize both images to extract the contours of the stripe pattern and cut both sides of the contours at predetermined positions (see Fig. 8).
Step 4) Overlap the two contour images by adjusting their positions.
Step 5) Determine the maximum difference between the corresponding contours (see Fig. 9).
Step 6) If the maximum difference is larger than $visibility$, assign the maximum difference to $visibility$.
Step 7) Shift the striped pattern of the light source by a predetermined minute amount. The procedure ends when the total shift exceeds the wavelength of the striped pattern. Otherwise, return to Step 2.

The $visibility$ obtained above represents the maximum distortion of the striped pattern, and this value was used to evaluate the defect visibility. To confirm the validity of this evaluation value, two inspectors engaged in a visual inspection and were shown the defect images generated by the simulation and asked to rate the visibility of the defect. Because the results of this evaluation and the trend of the $visibility$ values were consistent, this evaluation method was verified as valid and was applied to the experiments described in Section III.

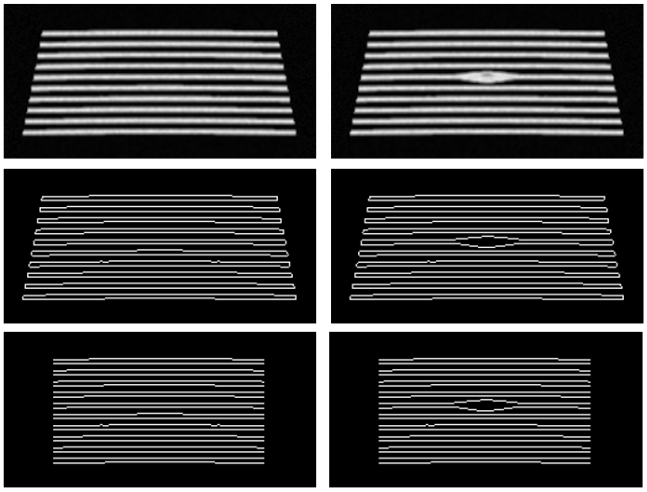

Fig. 8 (Left) Images of a normal surface. (Right) Images of defects on the same surface. (From top to bottom) Original images, contour images, and contour images cut on both sides.

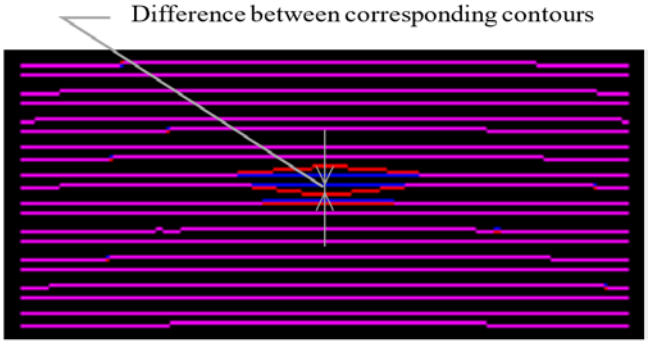

Fig. 9 RGB image of the two merged images in the lower portion of Fig. 8. The blue image shows the stripe-pattern contour reflected on normal surface and the red image shows the contour of the defective surface. The line where these two contours overlap is magenta. This figure shows a difference between corresponding contours.

III. Experiments

First, we describe the setup of the simulation model used in the experiments. The positional relationship between the light source and the camera was determined as follows: With reference to study [17], $d_{max} = 0.005\,mm$ and $\sigma^2 = 4.0\,mm^2$ were assumed as the size of a shallow defect that is difficult to visualize, and a positional relationship where this defect can be well visualized with a camera of 1024 × 1024 pixels (pixel pitch: 0.005 mm) with a lens with a focal length of 25 mm and a light source with a stripe spacing of 2.0 mm at an angle of 45° each was determined by using the simulation. The distances from the origin of the coordinate system to the principal points of the camera lens and light source were 175.6 mm and 256.0 mm, respectively. However, when the surface to be inspected was spherical, the stripe spacing of the light source was set as 10.0 mm to ensure the spacing of the reflected stripes.

In the case of bright-field illumination, the relationship between the light source and camera is that of specular reflection. Therefore, for example, if the camera distance is changed, the defect can be visualized in the same manner as before the distance change by changing the overall size, including the stripe spacing, in proportion to the change. Therefore, we believe that the conclusions drawn from the results of the experiments performed on the positional relationship described here are general as they hold at different scales.

In the simulation experiment, a defect was placed on each of the three test surfaces: a flat plate, a cylindrical surface (radius 70 mm), and a spherical surface (radius 70 mm), and the defect visibility evaluation was performed while changing the defect size and the angle of the camera's line of sight (θ: see Fig. 6). The shift in Step 7 of the evaluation method was set to 0.25 mm. The analytical parameter settings for the simulations are listed in Table 1.

For all combinations of the parameters listed in Table 1, the imaging was simulated on flat, cylindrical, and spherical surfaces, and the results were evaluated using the defect visibility evaluation method. The results for the flat, cylindrical, and spherical cases are shown in Fig. 10 to Fig. 13, Fig. 14 to Fig. 17, and Fig. 18 to Fig. 21, respectively. Fig. 10, 11, 14, 15, 18, and 19 show the images when the maximum difference was obtained by shifting the stripe pattern.

Table 1 Analyzed parameters.

θ (degree)	85.0, 75.0, 65.0, 55.0, 45.0, 35.0, 25.0, 15.0, 5.0
σ^2 (mm^2)	1.0, 4.0, 9.0, 16.0
d_{max} (mm)	0.003, 0.005

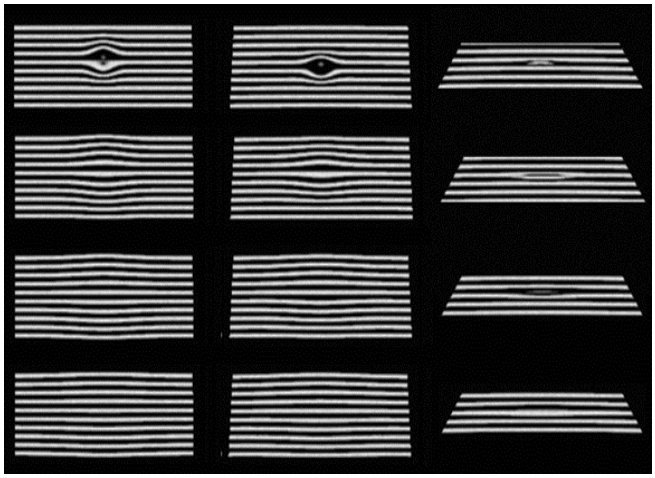

Fig. 10 Images of the flat surface with a defect of $d_{max} = 0.005$. (Left to Right) $\theta = 85.0, 45.0, 5.0$. (Top to Bottom) $\sigma^2 = 1.0, 4.0, 9.0, 16.0$.

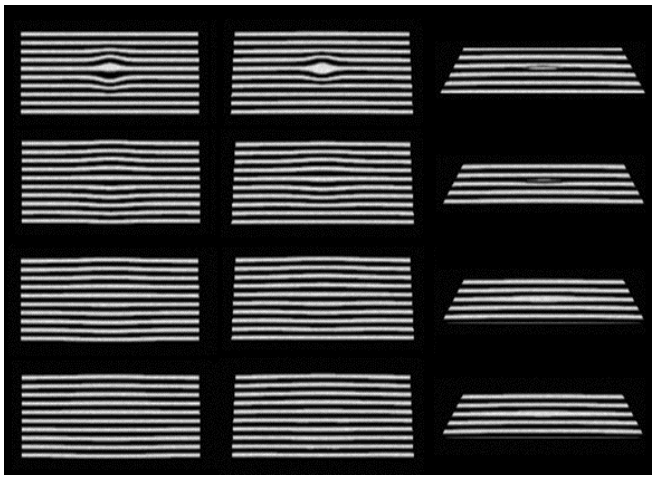

Fig. 11 Images of the flat surface with a defect of $d_{max} = 0.003$. (Left to Right) $\theta = 85.0, 45.0, 5.0$. (Top to Bottom) $\sigma^2 = 1.0, 4.0, 9.0, 16.0$.

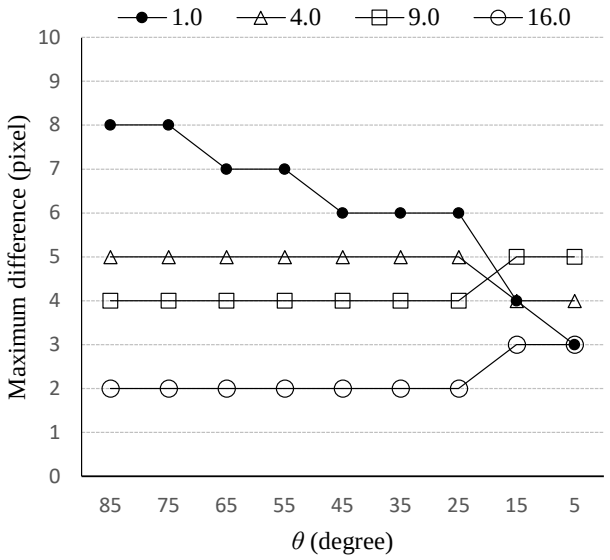

Fig. 12 Relationship between θ and the maximum difference for flat surfaces with a defect ($d_{max} = 0.005$) of $\sigma^2 = 1.0, 4.0, 9.0$, and 16.0.

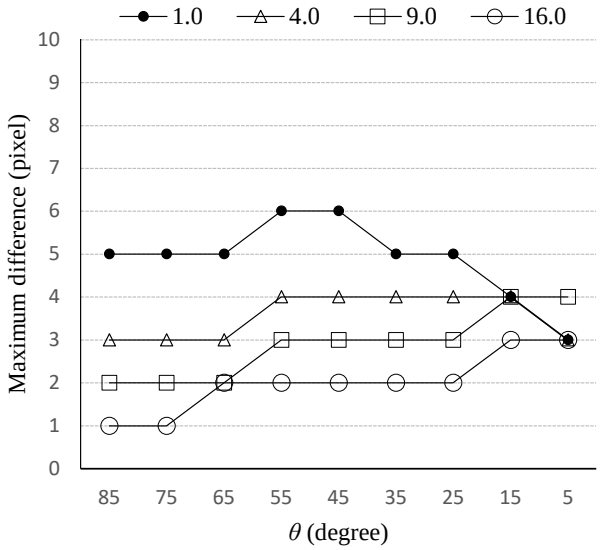

Fig. 13 Relationship between θ and the maximum difference for flat surfaces with a defect ($d_{max} = 0.003$) of $\sigma^2 = 1.0, 4.0, 9.0$, and 16.0.

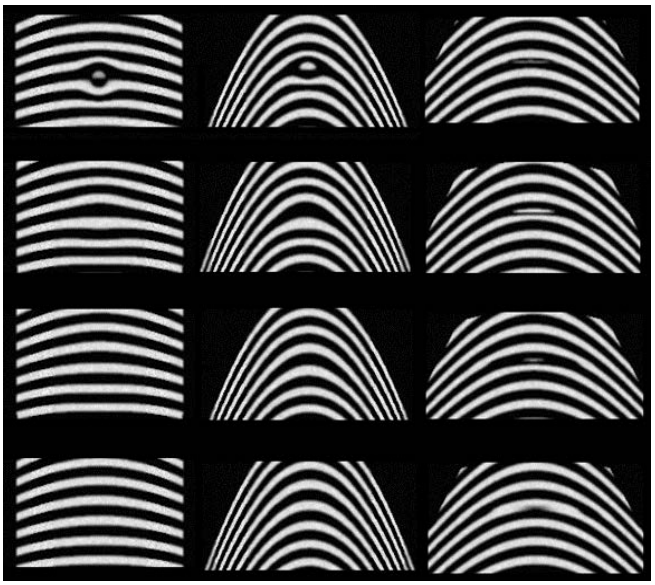

Fig. 14 Images of the cylindrical surface with defect of $d_{max} = 0.005$. (Left to Right) $\theta = 85.0, 45.0, 5.0$. (Top to Bottom) $\sigma^2 = 1.0, 4.0, 9.0, 16.0$.

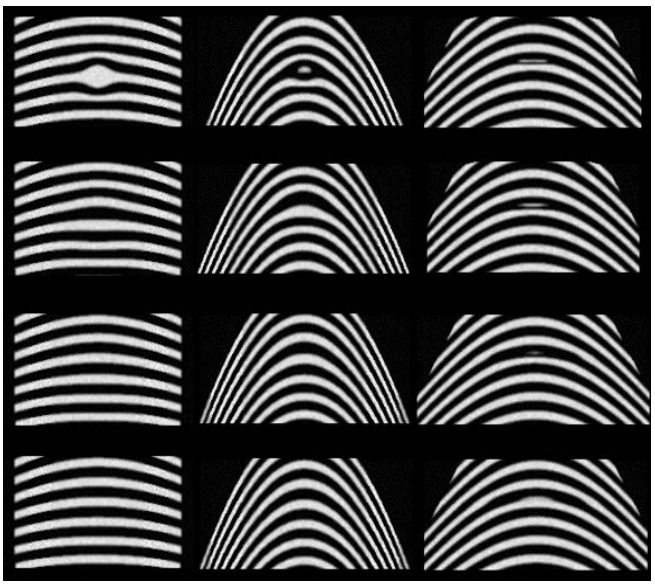

Fig. 15 Images of the cylindrical surface with defect of $d_{max} = 0.003$. (Left to Right) $\theta = 85.0, 45.0, 5.0$. (Top to Bottom) $\sigma^2 = 1.0, 4.0, 9.0, 16.0$.

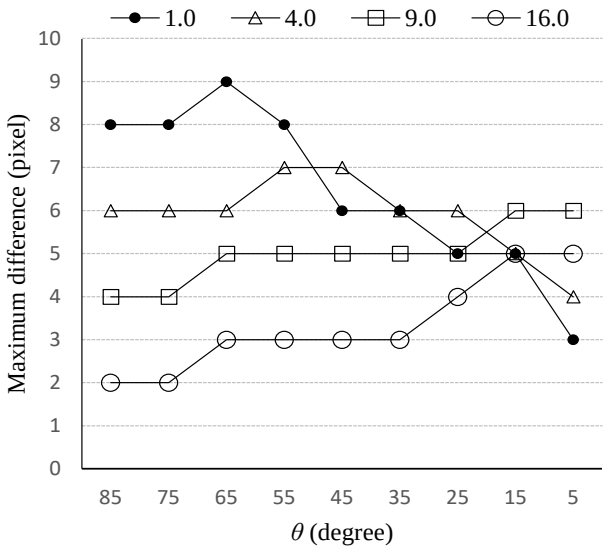

Fig. 16 Relationship between θ and the maximum difference for cylindrical surfaces with a defect ($d_{max} = 0.005$) of $\sigma^2 = 1.0, 4.0, 9.0$, and 16.0.

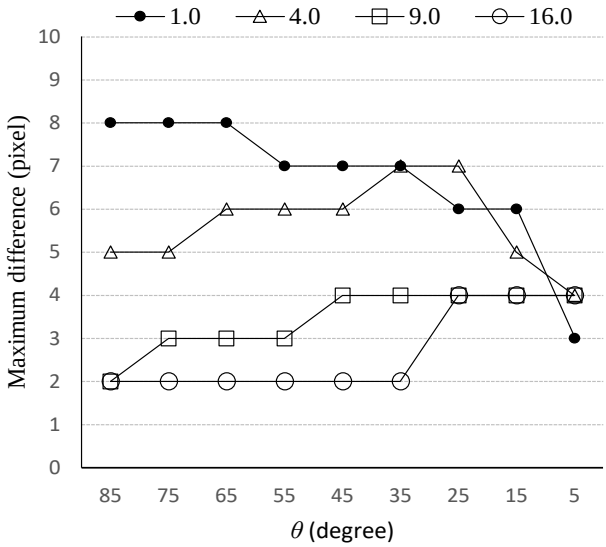

Fig. 17 Relationship between θ and the maximum difference for cylindrical surfaces with a defect ($d_{max} = 0.003$) of $\sigma^2 = 1.0, 4.0, 9.0$ and, 16.0.

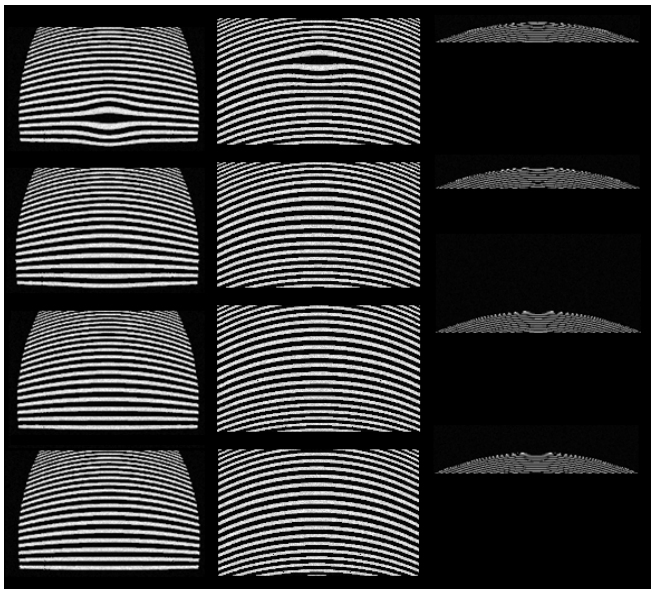

Fig. 18 Images of the spherical surface with a defect of $d_{max} = 0.005$. (Left to Right) $\theta = 85.0, 45.0, 5.0$. (Top to Bottom) $\sigma^2 = 1.0, 4.0, 9.0, 16.0$.

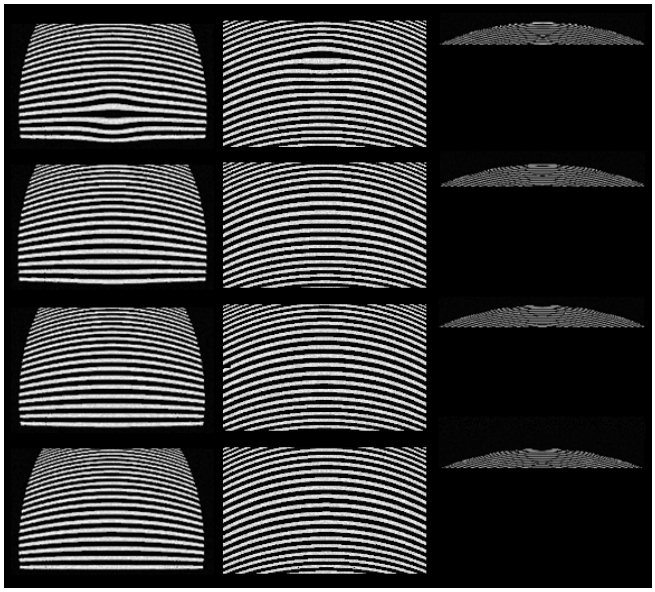

Fig. 19 Images of the spherical surface with a defect of $d_{max} = 0.003$. (Left to Right) $\theta = 85.0, 45.0, 5.0$. (Top to Bottom) $\sigma^2 = 1.0, 4.0, 9.0, 16.0$.

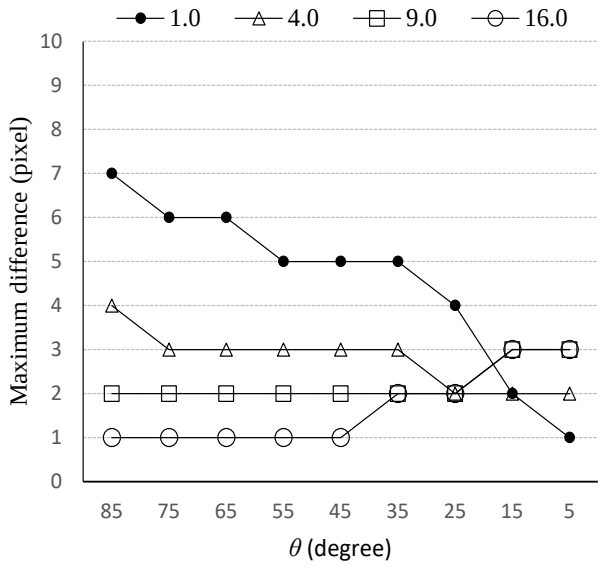

Fig. 20 Relationship between θ and the maximum difference for spherical surfaces with a defect ($d_{max} = 0.005$) of $\sigma^2 = 1.0, 4.0, 9.0$, and 16.0.

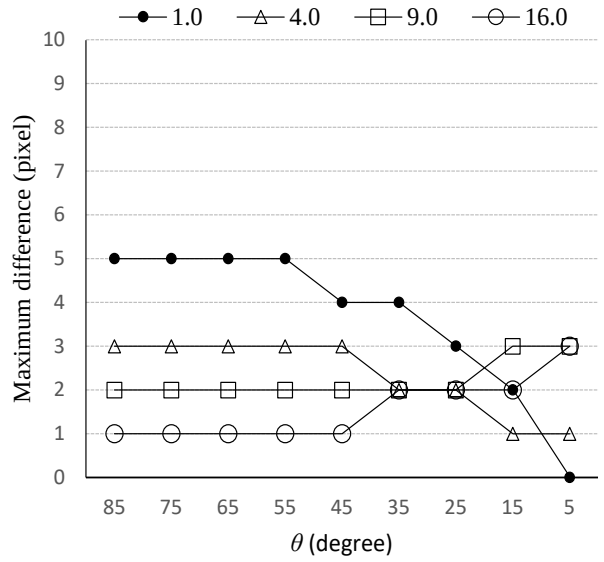

Fig. 21 Relationship between θ and the maximum difference for spherical surfaces with a defect ($d_{max} = 0.003$) of $\sigma^2 = 1.0, 4.0, 9.0$, and 16.0.

IV. Discussions

When the test surface is a flat plate, comparing the line graphs of the same type in Fig. 12 and 13, the greater the defect depth (d_{max}), the greater the distortion, that is, the more visible the defect. This is because the deeper the defect, the steeper the slope of the defect, and the greater the change in the normal direction, the greater the shift in the reflection direction. This is mostly true for cylindrical and spherical surfaces (Fig. 16 and 17, and Fig. 20 and 21).

Next, the comparison between the line graphs of the different types in each figure (i.e. comparison between the different σ^2) shows that, overall, the larger the σ^2, the smaller the distortion and the harder it is to see the defects. The reason for this is that, at constant depth, the larger the σ^2, the larger the diameter of the defect and therefore the sloping of the defect is more gradual. However, when the σ^2 is large ($\sigma^2 = 9.0, 16.0$), the distortion increases as θ decreases, making the defect more visible. In other words, the effect of "looking from just above the surface" is apparent for defects with a gentle slope.

On the other hand, for small values of σ^2 ($\sigma^2 = 1.0, 4.0$), defects become less visible as θ becomes smaller. It can therefore be seen that "looking from just above the surface" is effective for defects with a gentle slope. Defects with a steep slope, on the other hand, are better seen from a high angle. The same is true for flat, cylindrical, or spherical surfaces. These are the answers to the research questions presented in Section I.

The relationship between θ and σ^2 on defect visibility can be explained as follows: Fig. 22 and 23 show illustrations of the imaging of a concave defect with large and small σ^2, respectively. The two lines of sight of the camera in each figure originate from two adjacent pixels on the image sensor. A pinhole lens was used. In each figure, the top plot represents "looking from just above the surface."

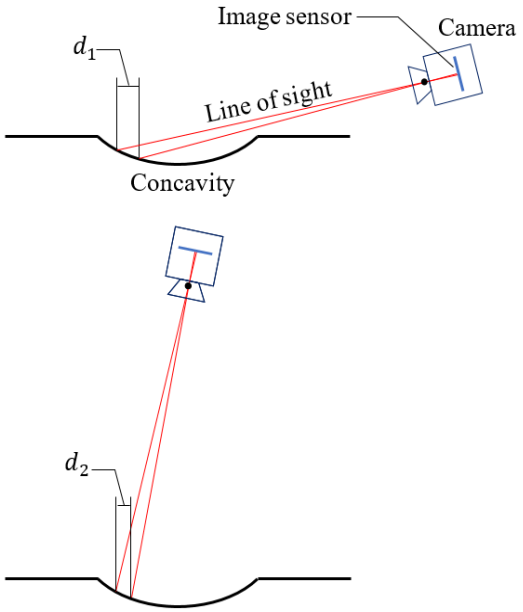

Fig. 22 Illustration of the imaging of a concave defect with a large diameter. The upper figure shows the case where θ is small and the lower one where θ is large.

As shown in Fig. 22, when σ^2 is large, the distance between the two points on the slope of the defect viewed by

the two lines of sight is greater for smaller θ ($d_2 < d_1$ in the figure). As a result, the distortion of the stripe pattern is considered to be greater when θ is smaller because the difference in the normal direction of the two points is greater. On the other hand, Fig. 23 shows that when σ^2 is small, the smaller the value of θ, the smaller the distortion. This is because the smaller diameter of the defect reduces the number of lines of sight affected by the defect as θ is smaller. However, these hypotheses must be verified experimentally.

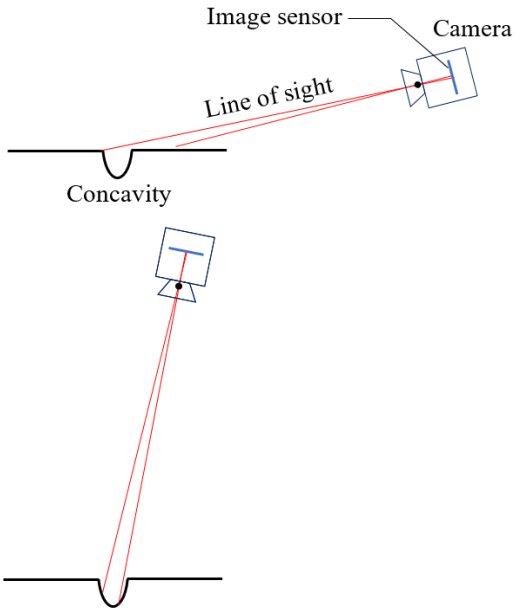

Fig. 23 Illustration of the imaging of a concave defect with a small diameter. The upper figure shows the case where θ is small and the lower one where θ is large.

V. Conclusion

It is known from experience that when a person inspects a surface, it is easier to see slight irregularities by "looking from just above the surface." This study confirmed the validity of this empirical knowledge through an optical simulation analysis of shallow concave defects. These results are general because they were confirmed on flat, cylindrical, and spherical surfaces, which are commonly found in industrial products.

Future work includes experimental verification of the hypothetical mechanism described in the discussion.

References

[1] R. Mordia and A. K. Verma, "Visual Techniques for Defects Detection in Steel Products: A Comparative Study," *Engineering Failure Analysis*, vol. 134, 106047, 2022.

[2] G Dong, S Sun, Z Wang, N Wu, P Huang, H Feng, and M. Pan, "Application of Machine Vision-Based NDT Technology in Ceramic Surface Defect Detection – A Review," *Materials Testing*, vol. 64, no. 2, pp. 202-21, 2022.

[3] A. Saberironaghi, J. Ren, and M. El-Gindy, "Defect Detection Methods for Industrial Products Using Deep Learning Techniques: A Review," *Algorithms*, vol. 16, no. 2, 95, 2023.

[4] Z. Wang and W. Liu, "Surface Defect Detection Algorithm for Strip Steel Based on Improved YOLOv7 Model," *IAENG International Journal of Computer Science*, vol. 51, no. 3, pp. 308-316, 2024.

[5] L.-P. Huang, Q.-C. Hsu, B.-H. Liu, C.-F. Lin, and C.-H. Chen, "Light Source Modules for Defect Detection on Highly Reflective Metallic Surfaces," *Metals*, vol. 13, 861, 2023.

[6] L. Arnal., E. Solanes, J. Molina, and J. Tornero, "Detecting Dings and Dents on Specular Car Body Surfaces Based on Optical Flow," *Journal of Manufacturing Systems*, vol. 45, pp. 306-321, 2017.

[7] S. Akhtar1, A. Tandiya, M. Moussa1, and C. Tarry, "A Robotics Inspection System for Detecting Defects on Semi-specular Painted Automotive Surfaces," in *Proc. ICRA2020*, Paris, France, 2020.

[8] L. Rosenboom, T. Kreis, and W. Jüptner "Surface Description and Defect Detection by Wavelet Analysis," *Measurement Science and Technology*, vol. 22, 045102, 2011.

[9] A. Hahn, M. Ziebarth, M. Heizmann, and A. Rieder, "Defect Classification on Specular Surfaces Using Wavelets," *Scale Space and Variational Methods in Computer Vision, Lecture Notes in Computer Science*, vol. 7893, 2013.

[10] T.-T. Le, M. Ziebarth, T. Greiner, and M. Heizmann, "Systematic Design of Object Shape Matched Wavelet Filter Banks for Defect Detection," in *Proc. 39th International Conference on Telecommunications and Signal Processing*, Vienna, Austria, pp. 470-473, 2016.

[11] T. Kreis, J. Burke, and R. B. Bergmann, "Surface Characterization by Structure Function Analysis," *Journal of the European Optical Society - Rapid Publications*, vol. 9, 14032, 2014.

[12] J. Guan, J. Fei, W. Li, X. Jiang, L. Wu, Y. Liu, and J. Xi, "Defect Classification for Specular Surfaces Based on Deflectometry and Multi-Modal Fusion Network," *Optics and Lasers in Engineering*, vol. 163, 107488, 2023.

[13] L. Fan, Z.Wu, J.Wang, C.Wei, H. Yue, and Y. Liu, "Deep Learning-Based Phase Measuring Deflectometry for Single-Shot 3D Shape Measurement and Defect Detection of Specular Objects," *Optics Express*, vol. 30, no. 15, 26504, 2022.

[14] M. T. Nguyen, Y.-S. Ghim, and H.-G. Rhee, "DYnet++: A Deep Learning Based Single-Shot Phase-Measuring Deflectometry for the 3-D Measurement of Complex Free-Form Surfaces," *IEEE Transactions on Industrial Electronics*, vol. 71, no. 2, pp. 2112-2121, 2024.

[15] P. Beckmann and A. Spizzichino, *The Scattering of Electromagnetic Waves from Rough Surfaces*, chapter 5, Oxford: Pergamon Press, 1963.

[16] T. Oshige and T. Koshihara, "Optical Characteristics of Concave and Convex Defects on Steel Sheets for Low-angle Incident Light and Its Application to Defect Inspection," *Transactions of the Society of Instrument and Control Engineers*, vol. 50, no. 9, pp. 640-645, 2014.

[17] O. Hirose, A. Ishii, S. Hata, and I. Washizaki, "Detection of Small Convex and Concave Defects on Optical Films by Patterned Illumination (2nd Report) - Estimation of Defect Detection by using Ray Tracing Method," *Journal of the Japan Society of Precision Engineering*, vol. 67, no. 7, pp. 1135-1139, 2001.

[18] Y. Xu, F. Gao, and X. Jiang, "Performance Analysis and Evaluation of Geometric Parameters in Stereo Deflectometry," *Engineering*, vol. 4, no. 6, pp. 806-815, 2018.

[19] H. Hana, S. Wu, and Z. Song, "Curved LCD Based Deflectometry Method for Specular Surface Measurement," *Optics and Lasers in Engineering*, vol. 151, 106909, 2022.

[20] A. S. Glassner (ed), An Introduction to Ray Tracing, Academic Press, New York, USA, 1989.

[21] J. F. Blinn, "Models of Light Reflection for Computer Synthesized Pictures," in *Proc. SIGGRAPH '77*, California, USA, 1977.